Published on 20 10 2016. Downloaded by Agency for Science, Technology & Research (A*STAR) on 2020-05-19 12:40:55.

RSC Advances

PAPER

View Article Online
View Journal | View Issue

Cite this: *RSC Adv.*, 2016, **6**, 102172

First principles studies on the thermoelectric properties of $(SrO)_m(SrTiO_3)_n$ superlattice

Liang Zhang,[a] Tie-Yu Lü,[a] Hui-Qiong Wang,[ab] Wen-Xing Zhang,[c] Shuo-Wang Yang[c] and Jin-Cheng Zheng*[abd]

Received 3rd August 2016
Accepted 19th October 2016

DOI: 10.1039/c6ra19661f

www.rsc.org/advances

The electronic structures and thermoelectric properties of $(SrO)_m(SrTiO_3)_n$ superlattices have been investigated using first-principles calculations and the Boltzmann transport theory. Due to the much reduced dispersion along the *c*-axis, the thermoelectric properties for n-type superlattices are found to be highly anisotropic with the in-plane electrical conductivity with respect to relaxation time much higher than the out-of-plane one. The reduction of the in-plane Seebeck coefficient compared with $SrTiO_3$ results in a slightly reduced power factor with respect to relaxation time for n-type doped $(SrO)_m(SrTiO_3)_n$. However, both Seebeck coefficient and electrical conductivity with respect to relaxation time are relatively maintained for p-type doping, leading to a comparable power factor with respect to relaxation time. If the reduced thermal conductivity is taken into account, an improved *ZT* value can be expected for the $(SrO)_m(SrTiO_3)_n$ superlattice.

Introduction

Thermoelectric (TE) materials can convert thermal energy into electrical power directly. The performance of TE materials is evaluated by a dimensionless figure of merit $ZT = S^2\sigma T/\kappa$, where S is the Seebeck coefficient, σ is the electrical conductivity, T is the absolute temperature, and κ is the thermal conductivity. Oxide TE materials have attracted large attention due to their non-toxicity, high natural abundance and thermal stability.[1] These advantages over traditional heavy metal based alloys make oxides viable alternatives for TE applications. Among the n-type oxide TE materials, $SrTiO_3$ has drawn much interest because it exhibits a rather high *ZT* of 0.37 at 1000 K when doped with Nb.[2,3] Because of the easily tuned electrical conductivity and the high Seebeck coefficient contributed by the triple degenerated Ti 3d-t_{2g} conduction band, a power factor ($S^2\sigma$) of 1.5×10^{-3} W m^{-1} K^{-2} is achieved,[2,4] which is comparable to state of the art TE materials. However, the *ZT* is limited because the thermal conductivity (around 3 W m^{-1} K^{-1} at 1000 K) is about one order of magnitude larger than the typical TE materials like SnSe.[5] Thus, it is desirable to reduce the thermal conductivity while maintaining its high power factor. Superlattice has been proved to be an effective way to improve the *ZT* value of TE material.[6,7] $(SrO)_m(SrTiO_3)_n$ is a superlattice consisting of m layers of rock salt SrO and n layers of $SrTiO_3$ alternately stacking along the *c*-axis. The $m = 1$ case ($(SrO)_1(SrTiO_3)_n$), known as Ruddlesden–Popper (RP) phase,[8,9] is a natural superlattice, while the $n = 1$ case ($(SrO)_m(SrTiO_3)_1$) has been recently grown using Molecular Beam Epitaxy (MBE).[10] The thermoelectric properties of RP-phase $(SrO)_1(SrTiO_3)_n$ have been studied widely.[11–17] Results show that the thermal conductivity is effectively reduced due to the enhanced phonon scattering at the $SrO/SrTiO_3$ interface. Although the absolute Seebeck coefficient is lowered in most cases due to the distorted TiO_6 octahedra, it can be essentially maintained by the restoration of the TiO_6 octahedra through carefully chosen doping elements like Sm.[14] However the electrical conductivity is significantly reduced due to the insulated SrO layer. The highest *ZT* reported is 0.24 at 1000 K for 5% Gd-doped $(SrO)_1(SrTiO_3)_2$ ceramic,[11] which is still smaller than that of $SrTiO_3$. Although the electron transport should be anisotropic in $(SrO)_m(SrTiO_3)_n$ due to the tetragonal crystal structure, the directional dependent transport parameters are poorly understood due to the difficulty in the synthesis of single crystalline or textured ceramic $(SrO)_m(SrTiO_3)_n$. The only paper on a highly *c*-axis oriented $(SrO)_1(SrTiO_3)_2$ that we are aware of shows an enhanced power factor compared with that of the ceramic counterpart because of the improved electrical conductivity.[17] So it's necessary to explore the directional dependence of the transport properties of these $SrTiO_3$ based superlattice and explore the possibility of improving the thermoelectric performance.

Methods

Density functional theory (DFT) calculations were performed using the planewave pseudopotential method as implemented in Quantum ESPRESSO package.[18] Perdew–Burke–Ernzerhof

[a]*Department of Physics, Collaborative Innovation Center for Optoelectronic Semiconductors and Efficient Devices, Xiamen University, Xiamen 361005, China. E-mail: jczheng@xmu.edu.cn*

[b]*Xiamen University Malaysia, 439000 Sepang, Selangor, Malaysia*

[c]*Institute of High Performance Computing, Agency for Science, Technology and Research, 1 Fusionopolis Way, #16-16 Connexis, Singapore 138632, Republic of Singapore*

[d]*Fujian Provincial Key Laboratory of Theoretical and Computational Chemistry, Xiamen University, Xiamen 361005, China*

This journal is © The Royal Society of Chemistry 2016

Published on 20 10 2016. Downloaded by Agency for Science, Technology & Research (A*STAR) on 2020-05-19 12:40:55.

(PBE)[19] generalized gradient approximation (GGA) was used for the exchange-correlation function. Ultrasoft pseudopotentials[20] were used to describe the core electron. Sr 4s4p4d5s5p, Ti 3s3p4s3d, and O 2s2p orbitals were treated as valence orbitals. A kinetic energy cutoff of 50 Ry for the plane wave basis set and of 500 Ry for the charge density was used to ensure convergence. The structural optimization finished when the stress along each of the three directions was less than 10^{-8} kbar. A Monkhorst–Pack k point grid[21] of $15 \times 15 \times 15$ ($k_x \times k_y \times k_z$) was used to ensure the convergence of the self-consistent calculation for $SrTiO_3$, while for other superlattice, the length of k_z is shortened with respect to $1/c$ (c is the lattice constant along the c-axis). For a detailed description of the band structure, which is necessary for the transport calculation, the calculation was performed using a denser k-mesh of $30 \times 30 \times 30$ for $SrTiO_3$; for other superlattice, k_z is shortened as well. The transport coefficients were calculated using the Boltzmann transport theory within the rigid band and constant relaxation time approach as implemented in BoltzTraP code.[22] This approach has been successfully used to a wide range of thermoelectric materials.[23–25] With this approach, the electrical conductivity is calculated with respect to τ, whereas the Seebeck coefficient is given with no fitting parameters.

Results and discussions

Fig. 1 shows the schematic structure of the $(SrO)_m(SrTiO_3)_n$ homologous series investigated in this work. It can be viewed as alternatively stacking of m layers of the SrO rock-salt and n layers of the $SrTiO_3$ perovskite. The $(SrO)_1(SrTiO_3)_n$ series, known as Ruddlesden–Popper phase, is a natural superlattice, and artificial MBE grown $(SrO)_m(SrTiO_3)_1$ series with m up to 4 have been reported.[10] The calculated lattice constants are shown in Table 1, with some available experimental values included for comparison. The calculated lattice constant for $SrTiO_3$ is 3.932 Å, which is slightly larger than the experimental value of 3.905 Å.[26] This is because GGA often overestimates the bond length. As the ratio of SrO layer increases, a contraction of the lattice constants in ab plane can be seen. This is generally in agreement with experimental results.[10,27] For $(SrO)_1(SrTiO_3)_1$, the TiO_6 octahedra is a little stretched along the c-axis and the Ti–O bond in ab plane is a little shorter than the Ti–O bond along c-axis, which is in good agreement with experimental results.[16] Similar changes apply to $(SrO)_2(SrTiO_3)_1$. There are three different Ti–O bonds in $(SrO)_1(SrTiO_3)_2$, and the Ti ions in the center of the octahedra sit at the sites higher than those of the O ions in the ab plane with a Ti–O angle of 178.3°. The distorted TiO_6 will split the Ti-d band and influence the thermoelectric properties.

Table 1 Calculated and experimental values of lattice constants and bandgaps for $(SrO)_m(SrTiO_3)_n$

	a (Å)		c (Å)		Band gap (eV)	
	Cal.	Exp.	Cal.	Exp.	Cal.	Exp.
$SrTiO_3$	3.932	3.905[a]			1.85	3.15[e], 3.25[f]
$(SrO)_1(SrTiO_3)_4$	3.927	3.87[b]	36.137	35.6[d]	1.81	3.36[e]
$(SrO)_1(SrTiO_3)_3$	3.926	3.83[b]	28.267	28.1[d]	1.87	3.41[e]
$(SrO)_1(SrTiO_3)_2$	3.925	3.94[b]	20.429	20.35[d]	1.93	3.45[e]
$(SrO)_1(SrTO_3)_1$	3.910	3.88[c]	12.630	12.46[d]	2.01	3.48[e]
$(SrO)_2(SrTO_3)_1$	3.866	3.79[c]	8.908	9.14[c]	2.07	
$(SrO)_3(SrTO_3)_1$	3.840	3.75[c]	22.912	23.55[c]	2.11	
$(SrO)_4(SrTO_3)_1$	3.817	3.76[c]	14.021	14.6[c]	2.10	

[a] Ref. 26. [b] Ref. 27. [c] Ref. 10. [d] Ref. 31. [e] Ref. 29. [f] Ref. 28.

The electronic band structures of $SrTiO_3$, $(SrO)_1(SrTiO_3)_n$ ($n = 1, 2, 3, 4$) and $(SrO)_m(SrTiO_3)_1$ ($m = 2, 3, 4$) are shown in Fig. 2. Strontium titanate appears as a band insulator with a band gap of 1.85 eV, smaller than the experimental value of 3.15 eV (ref. 28) due to the well-known underestimation of the band gap by GGA. As can be found from Table 1, the band gap increases from 1.81 eV for $(SrO)_1(SrTiO_3)_4$ to 2.10 eV for $(SrO)_4(SrTiO_3)_1$ as the number of $SrTiO_3$ block decreases. This trend is in accordance with experimental results[29] and can be attributed to the large band gap (5.7 eV)[30] of the rock salt SrO crystal. The $(SrO)_1(SrTiO_3)_n$ ($n = 1, 2, 3, 4$) series has an indirect band gap while $(SrO)_m(SrTiO_3)_1$ ($m = 2, 3, 4$) series are found to be of direct band gap. The band structure shows a strong anisotropic character in the conduction band. An almost dispersionless band along Γ–Z direction (along the c-axis) is found, indicating

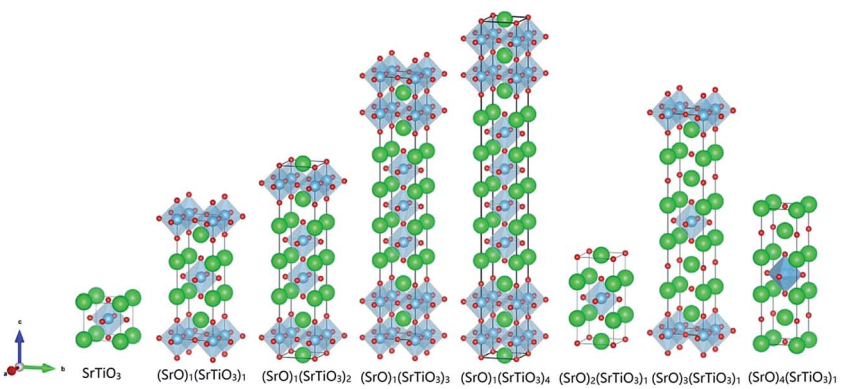

Fig. 1 Crystal structure of $(SrO)_m(SrTiO_3)_n$ homologous series.

Published on 20 10 2016. Downloaded by Agency for Science, Technology & Research (A*STAR) on 2020-05-19 12:40:55.

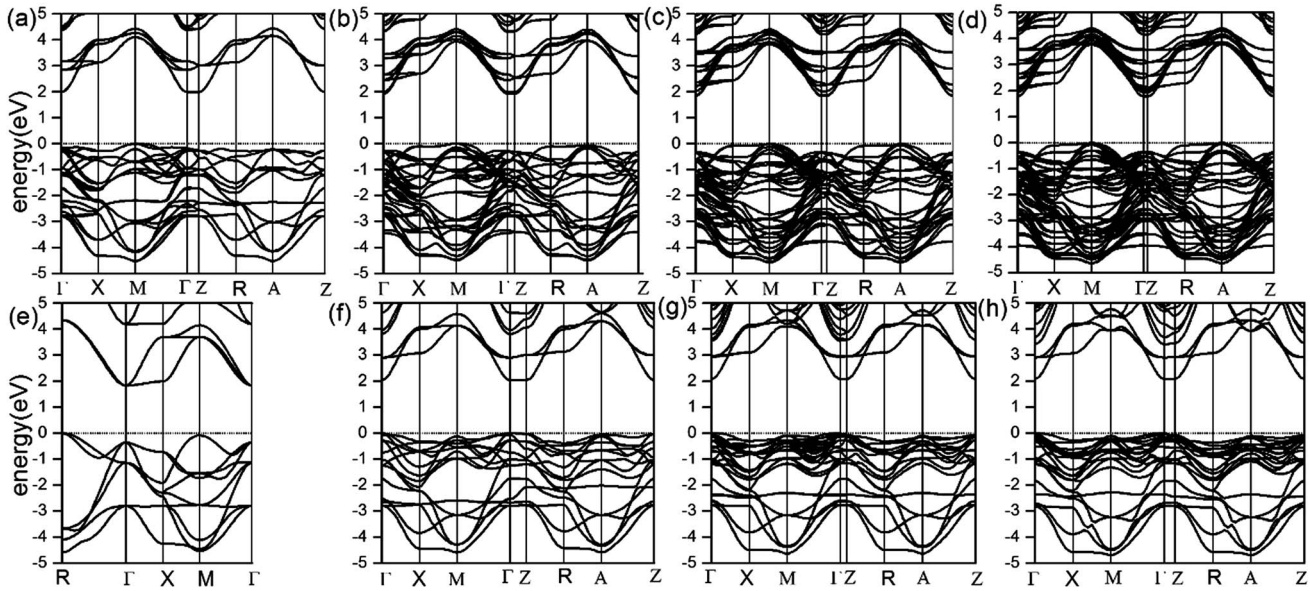

Fig. 2 Electronic band structures for (a) $(SrO)_1(SrTiO_3)_1$, (b) $(SrO)_1(SrTiO_3)_2$, (c) $(SrO)(SrTiO_3)_3$, (d) $(SrO)_1(SrTiO_3)_4$, (e) $SrTiO_3$, (f) $(SrO)_2(SrTiO_3)_1$, (g) $(SrO)_3(SrTiO_3)_1$, and (h) $(SrO)_4(SrTiO_3)_1$.

a poor electrical conductivity along this direction. Because of the distorted TiO_6 octahedra, the three degenerate t_{2g} state splits into d_{xy} and d_{yz} + d_{zx} states. The d_{xy} state is pushed downward and forms the bottom of the conduction band. Fig. 3 presents the total and partial electronic density of state (DOS). The valence band maximum (VBM) was set as zero for comparison. The conduction bands are mainly from Ti-d state while the valence band is dominated by O-2p state. We can find a sharp increase in DOS near the valence band edge, which is preferable for large Seebeck coefficient. The conduction band

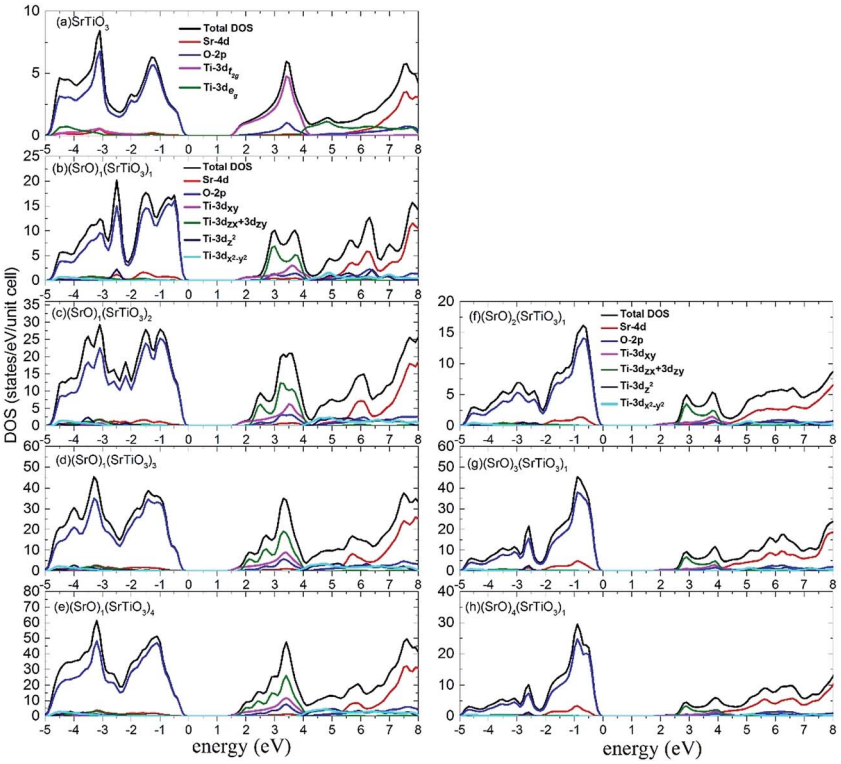

Fig. 3 Total and projected density of states for (a) $SrTiO_3$, (b) $(SrO)_1(SrTiO_3)_1$, (c) $(SrO)_1(SrTiO_3)_2$, (d) $(SrO)_1(SrTiO_3)_3$, (e) $(SrO)_1(SrTiO_3)_4$, (f) $(SrO)_2(SrTiO_3)_1$, (g) $(SrO)_3(SrTiO_3)_1$, and (h) $(SrO)_4(SrTiO_3)_1$.

 This journal is © The Royal Society of Chemistry 2016

Published on 20 10 2016. Downloaded by Agency for Science, Technology & Research (A*STAR) on 2020-05-19 12:40:55.

edge of $(SrO)_m(SrTiO_3)_n$ superlattice is characterized by a flat DOS, which is contributed by the Ti d_{xy} orbital of the splitted $d_{t_{2g}}$ states, followed by an abrupt increase in DOS. The slope of DOS near VBM is larger than that near conduction band minimum (CBM), which is favorable to Seebeck coefficient.[32] This indicates a larger S can be expected for hole doping, which is confirmed in our calculations.

To investigate the effect of interleaving the SrO or $SrTiO_3$ layers to the system, the thermoelectric properties as a function of chemical potential at 300 K are calculated and shown in Fig. 4. Within the rigid band approximation, the number of carrier is controlled by shifting the chemical potential and the negative and positive signs correspond to p-type and n-type doping respectively. The absolute Seebeck coefficient of $(SrO)_m(SrTiO_3)_n$ superlattice along the *xx*-direction decreases at a slope similar to that of $SrTiO_3$ when the chemical potential shifts away from the band gap. For the *zz*-direction, unusual small peaks are observed at the conduction band. By carefully observing the DOS, we found an abrupt increase at the corresponding energy, which is responsible for the increase of the absolute Seebeck coefficient because higher S can be achieved by increasing the energy dependence of DOS.[32] For RP phase series, increasing the $SrTiO_3$ layer will push the d_{yz+zx} bands downwards, thus causing the turn point of the DOS to move towards band edge as shown in the inset of Fig. 4(a). This will shift the peak of the Seebeck coefficient towards band edge. However, the position of the turn points near the conduction edge is insensitive to the number of SrO layer as illustrated in the inset of Fig. 4(e), resulting in an unchanged peak position for the $(SrO)_m(SrTiO_3)_1$ series. The SrO layer is served as barriers for the electrons across the plane and a two-dimensional band structure is expected for the conduction band, thus the electrical conductivity with respect to relaxation time (σ/τ, which will be referred to as "simplified electrical conductivity" hereafter) along the *xx*-direction is considerably larger than that along the *c*-axis for n-type doping. The peak values of the power factor with respect to relaxation time ($S^2\sigma/\tau$, which will be referred to as "simplified power factor" hereafter) of n-type doped $(SrO)_m(SrTiO_3)_n$ superlattice are smaller than that of $SrTiO_3$ as seen in Fig. 4(d) and (h). For p-type case, some structures exhibit larger maximum simplified power factor (MSPF) near the band edge, indicating promising thermoelectric performance for those structures.

The calculated doping level dependence of the thermoelectric properties at 300 K for RP phase series $(SrO)_1(SrTiO_3)_n$ and $(SrO)_m(SrTiO_3)_1$ series are shown in Fig. 5 and 6 respectively. The calculated absolute Seebeck coefficient continues to increase when the carrier concentration is lowered for all the structures, indicating the bipolar effect is not evident because of the large band gap.[33] S shows a Pisarenko behavior[24] with

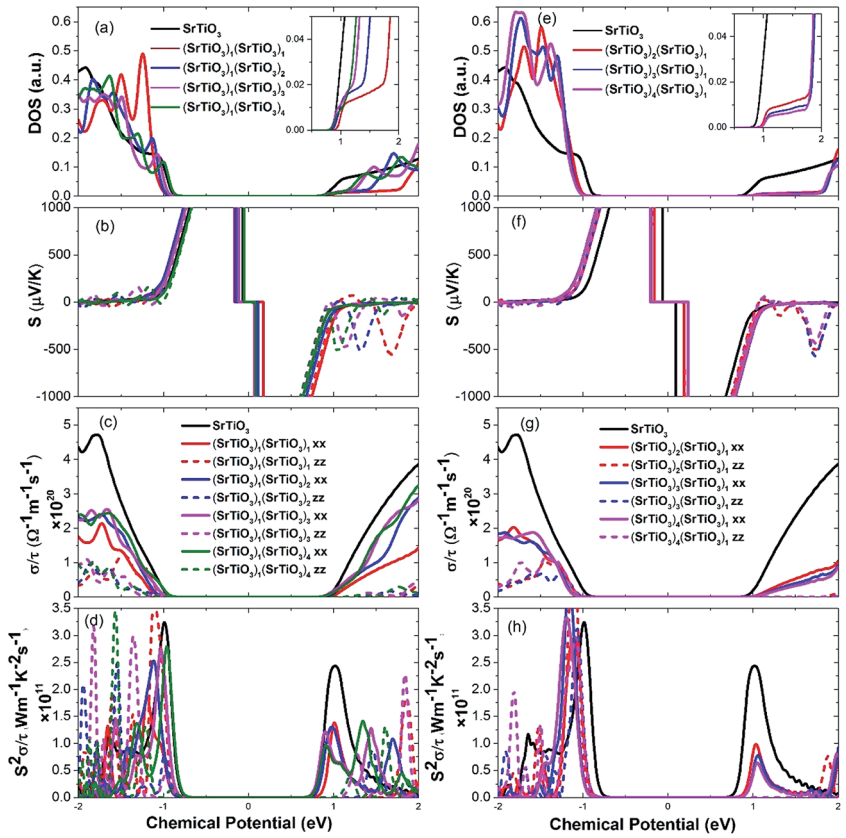

Fig. 4 Calculated results of the total density of states and thermoelectric properties (Seebeck coefficient (S), electrical conductivity with respect to relaxation time (σ/τ) and power factor with respect to relaxation time ($S^2\sigma/\tau$)) at 300 K for $(SrO)_1(SrTiO_3)_n$ series (left panel) and $(SrO)_m(SrTiO_3)_1$ series (right panel). The reference of chemical potential is set at the middle of the band gap.

Published on 20 10 2016. Downloaded by Agency for Science, Technology & Research (A*STAR) on 2020-05-19 12:40:55.

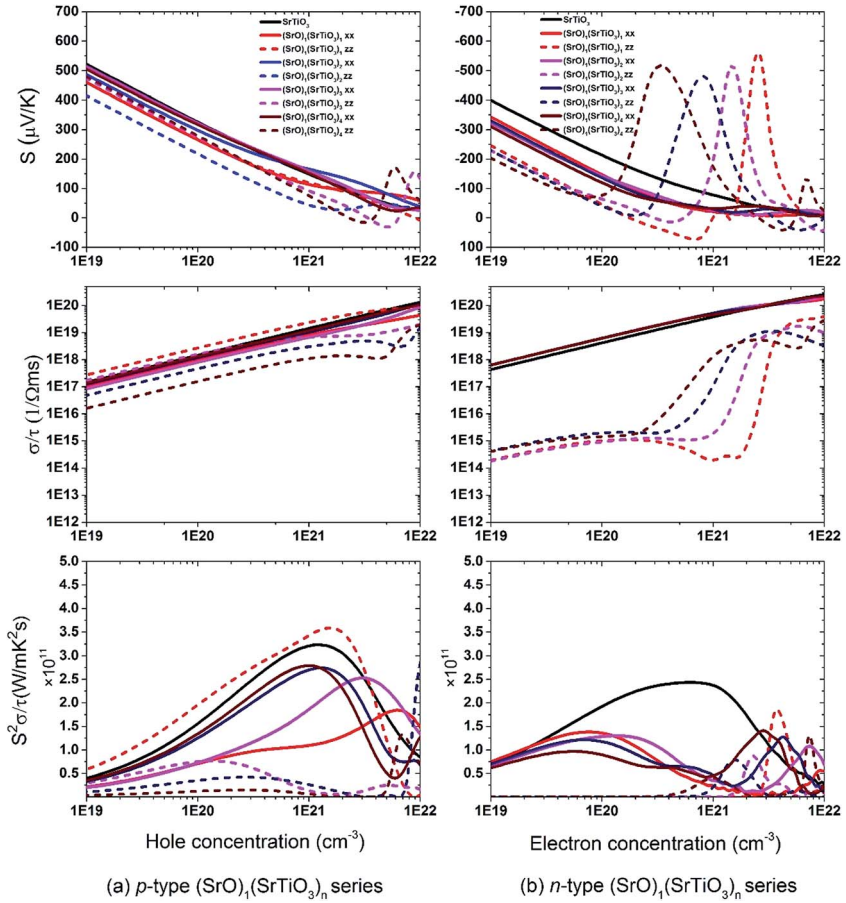

Fig. 5 Calculated thermoelectric properties for (a) p-type and (b) n-type RP phase $(SrO)_1(SrTiO_3)_n$ ($n = 1, 2, 3, 4$) compared with that of $SrTiO_3$ at 300 K as a function of carrier concentration.

a linear dependence of S on log of carrier concentration below doping level of 1×10^{20} cm^{-3}.

For n-type $SrTiO_3$, the calculated absolute Seebeck coefficient are in good agreement with other theoretical results[34–36,38] but are underestimated compared with experimental ones.[37] The discrepancy is likely due to the reduced bandwidth caused by the strong correlation effect of the Ti-3d states.[38] A highly anisotropic S can be found in electron doped RP phase $(SrO)_1(SrTiO_3)_n$ superlattice. The absolute Seebeck coefficient along the xx-direction ($|S_{xx}|$) is larger than that along the zz-direction ($|S_{zz}|$) at low carrier concentration and decreases monotonically with increasing carrier concentration. For $|S_{zz}|$, it decreases firstly and then increases drastically to about 500 μV K^{-1}, surpassing $|S_{xx}|$, and drops finally. The calculated absolute Seebeck coefficient values for $(SrO)_1(SrTiO_3)_1$ and $(SrO)_1(SrTiO_3)_2$ are smaller than that of $SrTiO_3$ when the carrier concentration is below 1×10^{21} cm^{-3}, which is in agreement with experimental results and can be attributed to the reduction of effective mass caused by the distorted TiO_6 octahedra.[16] Increasing the $SrTiO_3$ layer causes the peak to move towards lower carrier concentration. Although no reported experimental results are available, the p-type $SrTiO_3$ shows a larger Seebeck coefficient compared with n-type $SrTiO_3$ as can be expected from the larger slope of the DOS near the valence band edge. The p-type RP phase $(SrO)_1(SrTiO_3)_n$ exhibit larger Seebeck coefficient along the xx-direction, with the exception of $(SrO)_1(SrTiO_3)_1$, which shows an almost isotropic Seebeck coefficient. At high doping level, the Seebeck coefficient also shows a relative increase as the n-type counterpart but at a higher carrier concentration and with a more moderate rate. For $(SrO)_m(SrTiO_3)_1$ series, the n-type ones also have an unusual increase with its peak position moving towards lower doping level as SrO layer increases. For hole doping, the Seebeck coefficient continues to increase with increasing carrier concentration and at high doping level, the values for difference structures tend to converge.

The simplified electrical conductivity is sensitive to doping as shown in Fig. 5 and 6. The simplified electrical conductivity along the xx-direction is considerably lower than that along the zz-direction for n-type RP phase $(SrO)_1(SrTiO_3)_n$. σ_{xx}/τ_{xx} adopts a logarithm increase with doping while σ_{zz}/τ_{zz} undergoes an increase in increasing rate at doping level around 1×10^{21} cm^{-3} as bands with larger group velocity begin to set in. The σ_{xx}/τ_{xx} is three orders of magnitude larger than σ_{zz}/τ_{zz} at carrier concentration below 1×10^{20} cm^{-3}. At a higher concentration of 1×10^{22} cm^{-3}, the ratio decreased to one order. Experimentally, the electrical transport of a similar RP phase compound Sr_2RuO_4 has been studied,[39] and the in-plane electrical conductivity is

 This journal is © The Royal Society of Chemistry 2016

Published on 20 10 2016. Downloaded by Agency for Science, Technology & Research (A*STAR) on 2020-05-19 12:40:55.

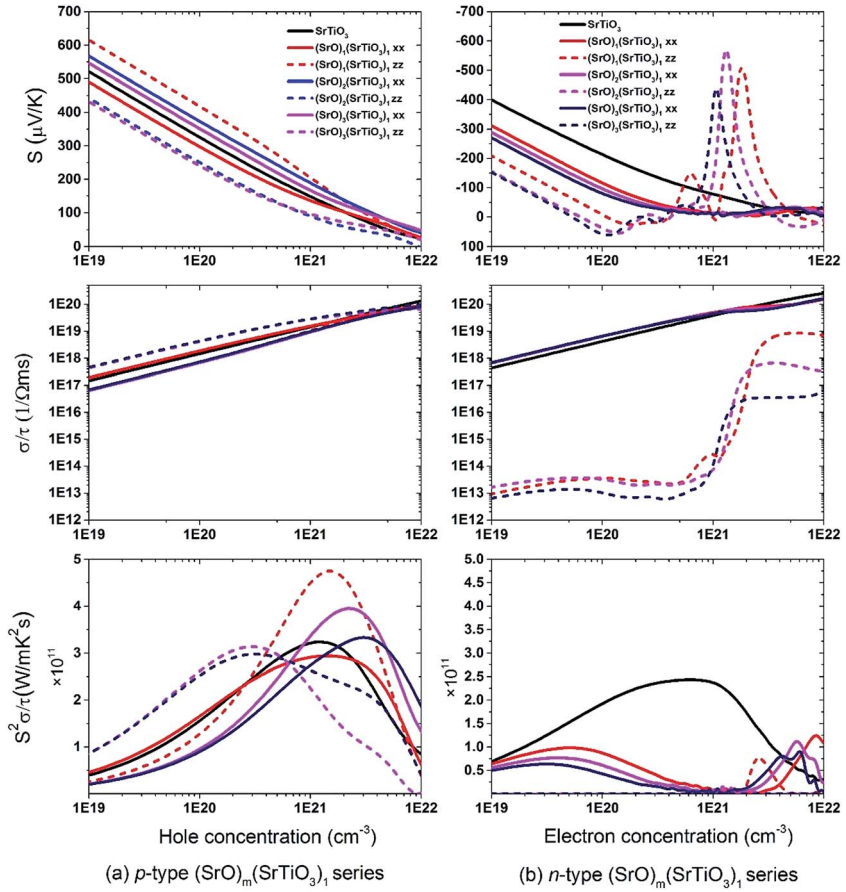

Fig. 6 Calculated thermoelectric properties for (a) p-type and (b) n-type $(SrO)_m(SrTiO_3)_1$ ($m = 2, 3, 4$) compared with that of $SrTiO_3$ at 300 K as a function of carrier concentration.

measured to be about two orders of magnitude larger than the out-of-plane case, which is in good agreement with our calculated result. The *xx* component of the simplified electrical conductivity is slightly larger than that of $SrTiO_3$ and is not sensitive to the variation of $SrTiO_3$ layer, while the *zz* component with more $SrTiO_3$ layers exhibits larger simplified electrical conductivity at high doping level. As for the n-type $(SrO)_m(SrTiO_3)_1$ series, the simplified electrical conductivity in the *zz*-direction is smaller than that of RP phase because of the larger band gap of SrO layer. At high doping level larger than 1×10^{21} cm^{-3}, as the insulating SrO layer increases, σ_{zz}/τ_{zz} decreases. The anisotropy for p-type case is not so remarkable with the simplified electrical conductivity along the two directions with the same order of magnitude. The simplified electrical conductivity for p-type case increases linearly with carrier concentration regardless of directions. The opposite effect of doping on S and σ/τ leads a subtle variation in simplified power factor. The MSPF is found at a doping level around 1×10^{21} cm^{-3} for n-type $SrTiO_3$, which is in agreement with experimental value. Two comparable MSPF along the *xx*-direction is observed for n-type RP phase $(SrO)_1(SrTiO_3)_n$ at carrier concentration around 1×10^{20} cm^{-3} and 1×10^{21} to 1×10^{22} cm^{-3} (depending on the structure), respectively. The reduction in MSPF compared with $SrTiO_3$ can be attributed to the reduced Seebeck coefficient. The optimal doping level for n-type RP phase along the *zz*-direction is in the range of 1×10^{21} cm^{-3} to 1×10^{22} cm^{-3} due to the increased simplified electrical conductivity and the local maximum of Seebeck coefficient in this range. The simplified power factor along the *xx*-direction for n-type $(SrO)_m(SrTiO_1)_1$ has the similar trend with two peaks being observed. The MSPF for n-type $(SrO)_2(SrTiO_1)_1$ along the *zz*-direction is observed at around 3×10^{21} cm^{-3}. As the increased SrO layer causes the simplified electrical conductivity to decrease drastically in the *zz*-direction, the MSPF become almost invisible in the graph. By examining the data, the MSPF are found to be in the doping range between 1×10^{21} cm^{-3} and 2×10^{21} cm^{-3}, with values one order of magnitude (for $m = 3$ case) and two orders of magnitude (for $m = 4$ case) smaller than that of $(SrO)_2(SrTiO_3)_1$. For p-type doping, the RP phase series have slightly smaller MSPF than $SrTiO_3$ along *xx*-direction, while $(SrO)_m(SrTiO_3)_1$ shows comparable MSPF with $SrTiO_3$ and larger MSPF are found in some certain structures. This suggests p-type $(SrO)_m(SrTiO_3)_1$ may have better thermoelectric performance than p-type $SrTiO_3$.

Fig. 7 and 8 shows the temperature dependence of the Seebeck coefficients at a carrier concentration of 1×10^{20} cm^{-3}. For n-type doping, the absolute Seebeck coefficient along different

Published on 20 10 2016. Downloaded by Agency for Science, Technology & Research (A*STAR) on 2020-05-19 12:40:55.

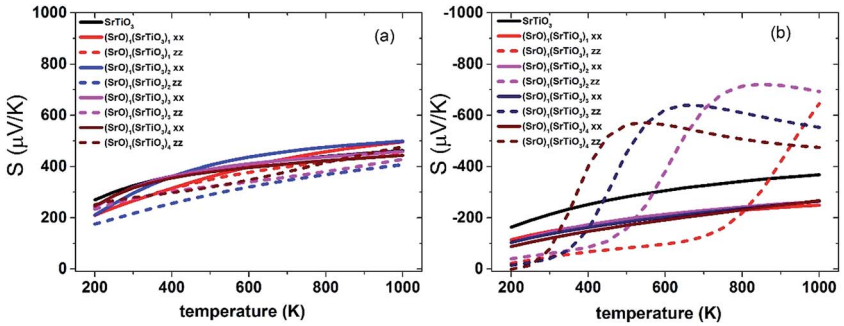

Fig. 7 Calculated temperature dependent Seebeck coefficient at carrier concentration of 1×10^{20} cm^{-3} for (a) p-type and (b) n-type RP phase $(SrO)_1(SrTiO_3)_n$ ($n = 1, 2, 3, 4$) series compared with that of $SrTiO_3$.

directions exhibit different temperature dependence. While $|S_{xx}|$ increases with increasing temperature linearly, $|S_{zz}|$ increased in a small rate first, then rapidly increased to a maximum value, and finally decreased. Experimentally, a small change in the increasing rate of S can be seen in $(SrO)_1(SrTiO_3)_1$ polycrystalline ceramic at around 700 K,[16] which can be attributed to the abrupt increase of $|S_{zz}|$. Structure with more $SrTiO_3$ layers is likely to reach the maximum $|S_{zz}|$ at lower temperature while $|S_{xx}|$ is insensitive to $SrTiO_3$ content. For p-type case, S increases monotonically with temperature regardless of the direction. The increasing rate varies between structures, resulting in some crossover of the Seebeck coefficient in the temperature range studied.

The calculated thermoelectric properties at carrier concentration of 1×10^{20} cm^{-3} along the xx-direction and the zz-direction at 300 K and 1000 K, as a function of the layer number of $SrTiO_3$ (n for RP phase $(SrO)_1(SrTiO_3)_n$ series) or SrO (m for $(SrO)_m(SrTiO_3)_1$ series) are shown in Fig. 9 and 10. For n-type $(SrO)_m(SrTiO_3)_n$, the absolute value of in-plane Seebeck coefficient is smaller than that of $SrTiO_3$ both at 300 K and 1000 K. For n-type RP phase, the absolute in-plane Seebeck coefficient changes slightly with n, while it decreases with increasing SrO number for n-type $(SrO)_m(SrTiO_3)_1$. $|S_{zz}|$ is smaller than $|S_{xx}|$ at 300 K, and as the temperature increases to 1000 K, it increases rapidly and exceeds $|S_{xx}|$. For $(SrO)_2(STiO_3)_1$, $|S_{zz}|$ reached a maximum of 920 μV K^{-1}, which is almost 3 times larger than that of $SrTiO_3$. Despite the significantly increased Seebeck coefficient, the power factor is still smaller because of the poor electrical conductivity. The variation of S for p-type Seebeck coefficient is a little complicated. S for $(SrO)_m(SrTiO_3)_n$ appears to oscillate around S value of $SrTiO_3$. S_{xx} is generally larger than S_{zz} except for some cases. Large anisotropic σ/τ is found for n-type $(SrO)_m(SrTiO_3)_n$ superlattice. While σ/τ along the layers almost remains unchanged when adding the insulating SrO layers, σ/τ decreases dramatically even with one layer of SrO added in every four $SrTiO_3$ units with $(\sigma_{xx}/\tau_{xx})/(\sigma_{zz}/\tau_{zz})$ equals 3000 and 100 at 300 K and 1000 K, respectively. The σ_{zz}/τ_{zz} value decreased monotonically with the increasing of the insulating SrO layer. For p-type case, the anisotropy is less profound. The σ/τ for p-type RP phase series along different directions shows different $SrTiO_3$ layer number dependence with the zz component increases with increasing of $SrTiO_3$ layer while the xx component exhibits the opposite trend. For $(SrO)_m(SrTiO_3)_1$ series, the σ/τ are found to oscillate around that of $SrTiO_3$. Interestingly, σ/τ perpendicular to the layers is even larger than that along the plane at some certain SrO layer number. The shape of the simplified power factor profile is similar with that of the σ/τ profile, suggesting the main factor that influences the relative value of the simplified power factor is the electrical conductivity. For n-type doping, the simplified power factor in the xx-direction is superior to that along the zz-direction in any case and is only slightly reduced from that of $SrTiO_3$. Experimentally, Lee *et al.* reported a highly enhanced power factor value for a highly c-axis-oriented $(SrO)_1(SrTiO_3)_1$ film (corresponding to the in-plane power factor) compared with

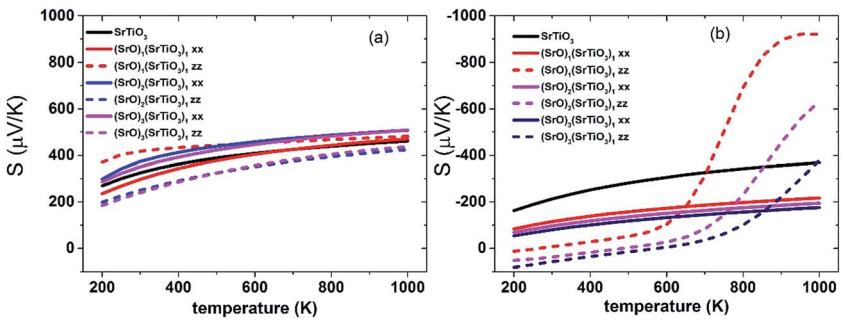

Fig. 8 Calculated temperature dependent Seebeck coefficient at carrier concentration of 1×10^{20} cm^{-3} for (a) p-type and (b) n-type $(SrO)_m(SrTiO_3)_1$ ($m = 2, 3, 4$) series compared with that of $SrTiO_3$.

 This journal is © The Royal Society of Chemistry 2016

Published on 20 10 2016. Downloaded by Agency for Science, Technology & Research (A*STAR) on 2020-05-19 12:40:55.

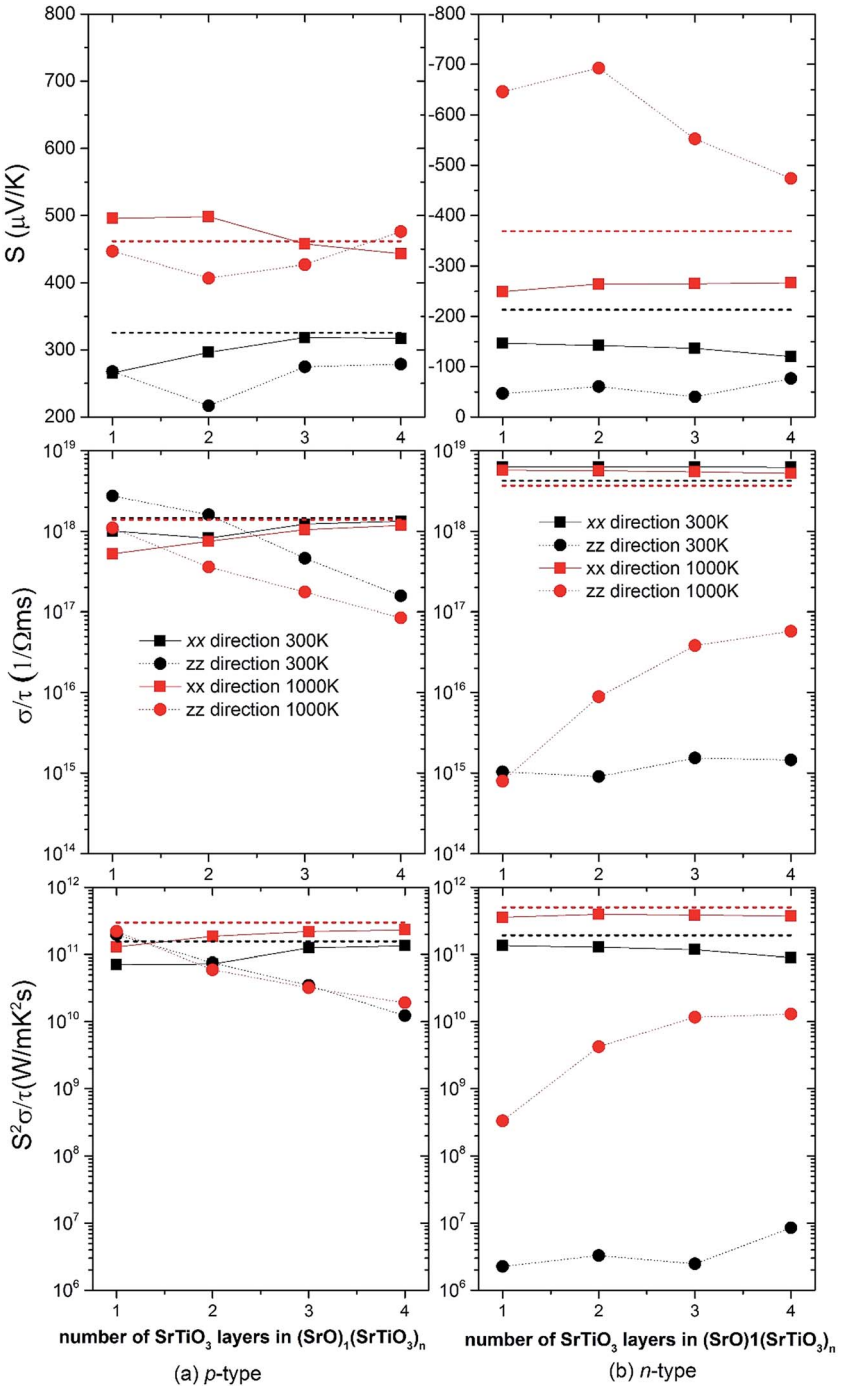

Fig. 9 Calculated thermoelectric properties along *xx*-direction and *zz*-direction at 300 K and 1000 K as a function of the number of $SrTiO_3$ layers for RP phase $(SrO)_1(SrTiO_3)_n$ ($n = 1, 2, 3, 4$) series. (a) p-Type doping and (b) n-type doping. The carrier concentration is set as 1×10^{20} cm^{-3} and the black and red horizontal dash lines represent the corresponding value for $SrTiO_3$ at 300 K and 1000 K, respectively.

$(SrO)_1(SrTiO_3)_1$ ceramic due to the increased electrical conductivity,[17] which is in accordance with our calculations. Molecular Dynamics (MD) simulation[40] shows the thermal conductivity parallel to the layer keeps decreasing when the SrO layer ratio increases. Assuming the relaxation time of the $(SrO)_m(SrTiO_3)_n$ superlattice is similar with that of $SrTiO_3$, a comparable *ZT* can be expected for $(SrO)_m(SrTiO_3)_n$ along the *xx*-direction. The simplified power factor for p-type $(SrO)_m(SrTiO_3)_n$ shows comparable values to $SrTiO_3$. Due to the reduced thermal conductivity, and assuming the relaxation time is comparable with that of $SrTiO_3$, a better *ZT* value can be expected if *m* and *n* are carefully chosen.

To gain more insight into the difference in anisotropy between the transport coefficient of n-type and p-type $(SrO)_m(SrTiO_3)_n$ superlattice, the Fermi surface (only one band is shown for illustration) at 300 K for p-type doping

Published on 20 10 2016. Downloaded by Agency for Science, Technology & Research (A*STAR) on 2020-05-19 12:40:55.

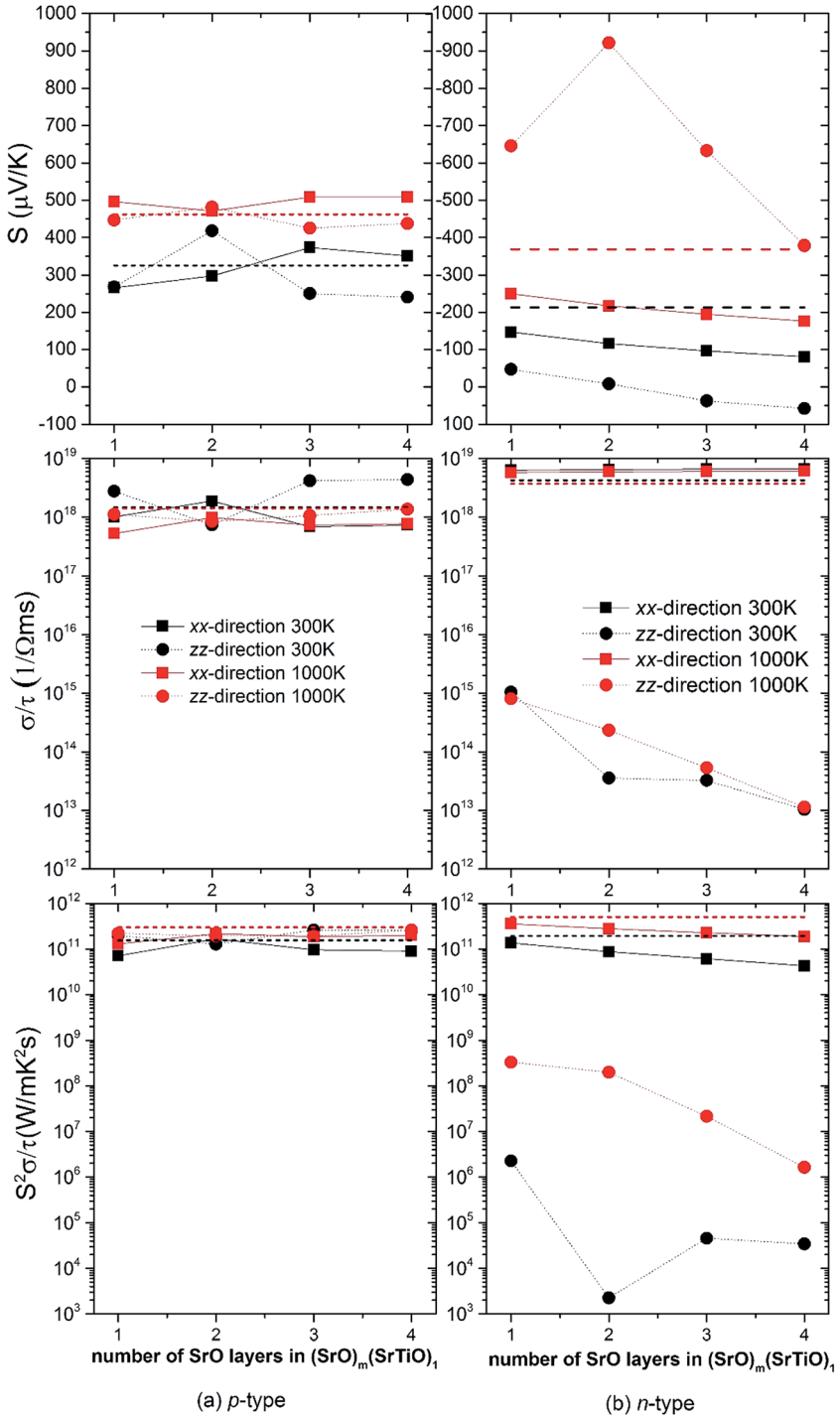

Fig. 10 Calculated thermoelectric properties along *xx*-direction and *zz*-direction at 300 K and 1000 K as a function of the number of SrO layers for $(SrO)_m(SrTiO_3)_1$ ($m = 2, 3, 4$) series. (a) p-Type doping and (b) n-type doping. The carrier concentration is set as 1×10^{20} cm^{-3} and the black and red horizontal dash lines represent the corresponding value for $SrTiO_3$ at 300 K and 1000 K, respectively.

(corresponding to a hole concentration of 1×10^{21} cm^{-3}) and n-type doping (corresponding to an electron concentration of 1×10^{21} cm^{-3}) of $SrTiO_3$ and $(SrO)_1(SrTiO_3)_1$ is plotted in Fig. 11. The Fermi surface of $SrTiO_3$ has six bulges along the three axes. For the n-type $(SrO)_1(SrTiO_3)_1$, the Fermi surface is cylindrical which is open in the direction of *c*-axis. As the group velocity of electrons is perpendicular to the Fermi surface, the in-plane simplified electrical conductivity is expected to be considerably larger than that along the *c*-axis. While for p-type doping, the ellipsoid shape of the Fermi surface indicates a less anisotropic behavior in electron transport.

 This journal is © The Royal Society of Chemistry 2016

Published on 20 10 2016. Downloaded by Agency for Science, Technology & Research (A*STAR) on 2020-05-19 12:40:55.

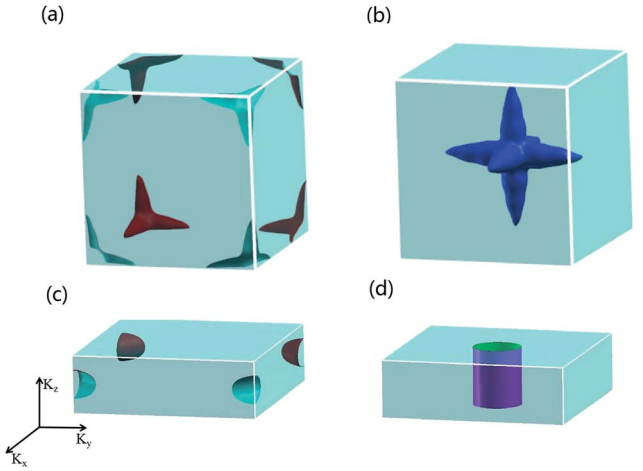

Fig. 11 Fermi surface corresponding to a carrier concentration of 1×10^{21} cm^{-3} at 300 K for (a) p-type $SrTiO_3$, (b) n-type $SrTiO_3$, (c) p-type $(SrO)_1(SrTiO_3)_1$ and (d) n-type $(SrO)_1(SrTiO_3)_1$.

Conclusion

In conclusion, we employed the first-principles DFT calculation and the Boltzmann transport theory to investigate the thermoelectric properties of $(SrO)_m(SrTiO_3)_n$. Due to the strong two dimensional character of the band structure near the CBM, the n-type $(SrO)_m(SrTiO_3)_n$ superlattices show strong anisotropy in thermoelectric properties: while the in-plane simplified electrical conductivity of n-type $(SrO)_m(SrTiO_3)_n$ is relatively maintained compared with that of $SrTiO_3$, the simplified electrical conductivity along the *c*-axis is significantly reduced, resulting in a much lower simplified power factor in this direction. Whereas for the p-type case small anisotropy for the transport coefficient is observed. Assuming the same relaxation time as $SrTiO_3$, a comparable power factor with that of $SrTiO_3$ can be achieved due to the relatively maintained Seebeck coefficient and electrical conductivity. Considering the reduced thermal conductivity, higher *ZT* can be expected if the layer numbers of SrO and $SrTiO_3$ blocks are optimized. Our results demonstrate the possibility of improving the thermoelectric performance of $SrTiO_3$ through atomic design and this approach can be applied to other oxide thermoelectric materials.

Acknowledgements

This work is supported by the Fundamental Research Funds for Central Universities (Grant No. 2013121010, 20720160020), the Natural Science Foundation of Fujian Province, China (Grant No. 2015J01029), Special Program for Applied Research on Super Computation of the NSFC-Guangdong Joint Fund (the second phase), the National Natural Science Foundation of China (no. U1332105, 11335006), and the National High-tech R&D Program of China (863 Program, No. 2014AA052202).

References

1 H. Ohta, *Mater. Today*, 2007, **10**, 44–49.
2 S. Ohta, T. Nomura, H. Ohta, M. Hirano, H. Hosono and K. Koumoto, *Appl. Phys. Lett.*, 2005, **87**, 092108.
3 N. Wang, H. Chen, H. He, W. Norimatsu, M. Kusunoki and K. Koumoto, *Sci. Rep.*, 2013, **3**, 3449.
4 B. Jalan and S. Stemmer, *Appl. Phys. Lett.*, 2010, **97**, 042106.
5 L. D. Zhao, S. H. Lo, Y. Zhang, H. Sun, G. Tan, C. Uher, C. Wolverton, V. P. Dravid and M. G. Kanatzidis, *Nature*, 2014, **508**, 373–377.
6 H. Ohta, S. Kim, Y. Mune, T. Mizoguchi, K. Nomura, S. Ohta, T. Nomura, Y. Nakanishi, Y. Ikuhara, M. Hirano, H. Hosono and K. Koumoto, *Nat. Mater.*, 2007, **6**, 129–134.
7 A. I. Abutaha, S. R. S. Kumar, K. Li, A. M. Dehkordi, T. M. Tritt and H. N. Alshareef, *Chem. Mater.*, 2015, **27**, 2165–2171.
8 S. N. Ruddlesden and P. Popper, *Acta Crystallogr.*, 1957, **10**, 538–539.
9 S. N. Ruddlesden and P. Popper, *Acta Crystallogr.*, 1958, **11**, 54–55.
10 P. Fisher, S. Wang, M. Skowronski, P. A. Salvador, M. Snyder and O. Maksimov, *Appl. Phys. Lett.*, 2007, **91**, 252901.
11 Y. Wang, K. H. Lee, H. Ohta and K. Koumoto, *J. Appl. Phys.*, 2009, **105**, 103701.
12 K. H. Lee, Y. F. Wang, S. W. Kim, H. Ohta and K. Koumoto, *Int. J. Appl. Ceram. Technol.*, 2007, **4**, 326–331.
13 Y. Wang, C. Wan, X. Zhang, L. Shen, K. Koumoto, A. Gupta and N. Bao, *Appl. Phys. Lett.*, 2013, **102**, 183905.
14 Y. Wang, K. H. Lee, H. Hyuga, H. Kita, H. Ohta and K. Koumoto, *J. Electroceram.*, 2010, **24**, 76–82.
15 K. H. Lee, S. W. Kim, H. Ohta and K. Koumoto, *J. Appl. Phys.*, 2007, **101**, 083707.
16 K. H. Lee, S. W. Kim, H. Ohta and K. Koumoto, *J. Appl. Phys.*, 2006, **100**, 063717.
17 K. H. Lee, A. Ishizaki, S. W. Kim, H. Ohta and K. Koumoto, *J. Appl. Phys.*, 2007, **102**, 033702.
18 P. Giannozzi, S. Baroni, N. Bonini, M. Calandra, R. Car, C. Cavazzoni, D. Ceresoli, G. L. Chiarotti, M. Cococcioni, I. Dabo, A. Dal Corso, S. de Gironcoli, S. Fabris, G. Fratesi, R. Gebauer, U. Gerstmann, C. Gougoussis, A. Kokalj, M. Lazzeri, L. Martin-Samos, N. Marzari, F. Mauri, R. Mazzarello, S. Paolini, A. Pasquarello, L. Paulatto, C. Sbraccia, S. Scandolo, G. Sclauzero, A. P. Seitsonen, A. Smogunov, P. Umari and R. M. Wentzcovitch, *J. Phys.: Condens. Matter*, 2009, **21**, 395502.
19 J. P. Perdew, K. Burke and M. Ernzerhof, *Phys. Rev. Lett.*, 1996, **77**, 3865–3868.
20 D. Vanderbilt, *Phys. Rev. B: Condens. Matter Mater. Phys.*, 1990, **41**, 7892–7895.
21 H. J. Monkhorst and J. D. Pack, *Phys. Rev. B: Solid State*, 1976, **13**, 5188–5192.
22 G. K. H. Madsen and D. J. Singh, *Comput. Phys. Commun.*, 2006, **175**, 67–71.
23 K. P. Ong, D. J. Singh and P. Wu, *Phys. Rev. B: Condens. Matter Mater. Phys.*, 2011, **83**, 115110.
24 M. S. Lee, F. P. Poudeu and S. D. Mahanti, *Phys. Rev. B: Condens. Matter Mater. Phys.*, 2011, **83**, 085204.
25 L. Xu, Y. Zheng and J. C. Zheng, *Phys. Rev. B: Condens. Matter Mater. Phys.*, 2010, **82**, 195102.

Published on 20 10 2016. Downloaded by Agency for Science, Technology & Research (A*STAR) on 2020-05-19 12:40:55.

26 T. Tomio, H. Miki, H. Tabata, T. Kawai and S. Kawai, *J. Appl. Phys.*, 1994, **76**, 5886–5890.
27 W. Tian, X. Q. Pan, J. H. Haeni and D. G. Schlom, *J. Mater. Res.*, 2001, **16**, 2013–2026.
28 K. V. Benthem, C. Elsässer and R. H. French, *J. Appl. Phys.*, 2001, **90**, 6156–6164.
29 C. H. Lee, N. J. Podraza, Y. Zhu, R. F. Berger, S. Shen, M. Sestak, R. W. Collins, L. F. Kourkoutis, J. A. Mundy, H. Wang, Q. Mao, X. Xi, L. J. Brillson, J. B. Neaton, D. A. Muller and D. G. Schlom, *Appl. Phys. Lett.*, 2013, **102**, 122901.
30 A. K. Vijh, *J. Mater. Sci. Lett.*, 1990, **9**, 609–610.
31 J. H. Haeni, C. D. Theis, D. G. Schlom, W. Tian, X. Q. Pan, H. Chang, I. Takeuchi and X. D. Xiang, *Appl. Phys. Lett.*, 2001, **78**, 3292–3294.
32 P. Qiu, J. Yang, X. Huang, X. Chen and L. Chen, *Appl. Phys. Lett.*, 2010, **96**, 152105.
33 J. J. Pulikkotil, D. J. Singh, S. Auluck, M. Saravanan, D. K. Misra, A. Dhar and R. C. Budhani, *Phys. Rev. B: Condens. Matter Mater. Phys.*, 2012, **86**, 155204.
34 K. Shirai and K. Yamanaka, *J. Appl. Phys.*, 2013, **113**, 053705.
35 D. Zou, Y. Liu, S. Xie, J. Lin and J. Li, *Chem. Phys. Lett.*, 2013, **586**, 159–163.
36 B. Amin, N. Singh, T. M. Tritt, H. N. Alshareef and U. Schwingenschlögl, *Appl. Phys. Lett.*, 2013, **103**, 031907.
37 S. Ohta, T. Nomura, H. Ohta and K. Koumoto, *J. Appl. Phys.*, 2005, **97**, 034106.
38 H. Usui, S. Shibata and K. Kuroki, *Phys. Rev. B: Condens. Matter Mater. Phys.*, 2010, **81**, 205121.
39 D. G. Schlom, S. B. Knapp, S. Wozniak, L. N. Zou, J. Park, Y. Liu, M. E. Hawley, G. W. Brown, A. Dabkowski, H. A. Dabkowska, R. Uecker and P. Reiche, *Supercond. Sci. Technol.*, 1997, **10**, 891–895.
40 A. Chernatynskiy, R. W. Grimes, M. A. Zurbuchen, D. R. Clarke and S. R. Phillpot, *Appl. Phys. Lett.*, 2009, **95**, 161906.

This journal is © The Royal Society of Chemistry 2016